JOURNAL OF NANO- AND ELECTRONIC PHYSICS
Vol. **17** No 1, 01009(6pp) (2025)

ЖУРНАЛ НАНО- ТА ЕЛЕКТРОННОЇ ФІЗИКИ
Том **17** № 1, 01009(6cc) (2025)

OPEN ACCESS

REGULAR ARTICLE

Structure, Morphology, and Multiferroic Properties of $Bi_{0.2}La_{0.8-x}Al_xFeO_3$ (x = 0.2, 0.4, 0.6 & 0.8) Nanoparticles

S. Perugu[1], G.B. Kiran[2,*] ✉, T.A. Bbau[3], B.V. Raghavaiah[4]

[1] *Department of Physics, Acharya Nagarjuna University, Guntur-522510, India*
[2] *Department of Mechanical Engineering, Rajiv Gandhi University of Knowledge Technologies (RGUKT), Nuzvid-521201, India*
[3] *Department of Physics, Andhra University, Visakhapatnam-530003, India*
[4] *Department of Physics, Rajiv Gandhi University of Knowledge Technologies (RGUKT), Ongole-523001, India*

(Received 25 November 2024; revised manuscript received 15 February 2025; published online 27 February 2025)

In this research work, $Bi_{0.2}La_{0.8-x}Al_xFeO_3$ (x = 0.2, 0.4, 0.6 & 0.8) (BLAFO) nanoparticles were prepared through hydrothermal technique. The trigonal phases were detected in the X-ray diffraction patterns. Secondary phases related to aluminum titanate and rutile were found. The FESEM and HRTEM images revealed the formation of nanorods-like structures due to the nucleation process. The dielectric properties expressed the space charge polarization and Debye-type relaxations in the frequency-dependent dielectric constant plots. Similarly, the dielectric versus frequency plots showed multiple relaxations. The magnetic hysteresis curves showed a decreasing trend in magnetization and magnetic moment. The LAS plots were shown to indicate the saturation magnetization. The ferroelectric hysteresis loops revealed the banana shape for all the samples.

Keywords: Nanoparticles, Multiferroic, Structure, Microscopy, Dielectric constant, Magnetic.

DOI: 10.21272/jnep.17(1).01009

PACS numbers: 78.67.Bf, 77.84. – s, 61.46. – w, 68.37.Hk, 78.20.Ci, 87.50.cm

1. INTRODUCTION

Multiferroic perovskite has predominant applications in science and technology, such as ferroelectric memory, charge storage, relaxor devices, etc. [1]. The dielectric, ferroelectric, and magnetic cations must be located among these multiferroic perovskites. For instance, $BiFeO_3$ consists of a multiferroic cation as Bi_3^+ and a magnetic cation as Fe_3^+. In the same fashion, the $BiMnO_3$ and $PbVO_3$ show a multiferroic nature.

Several scientists worked on doped bismuth ferrite reporting the phase transition, pressure-based phase transition, photocatalytic, optical band gap, microwave properties, electrochemical activity, and dielectric behavior of $BiLaFeO_3$, multiferroic nature of $BiLaFeTiO_3$ nanoparticles, ferroelectric transitions of $BiLaFeCoO_3$, multiferroic behavior of $BiLaCeO_3$, and magnetoelectric coupling nature of $BiSrNiO_3$ [1-10]. These reports were given by synthesizing and characterizing the $BiLaFeO_3$ and their co-doped materials. The literature survey showed that dopant/substituents like La, Co, Ce, Fe, Ti, Sr, Ni, Mn, V, etc., were added to bismuth ferrite. In this work, the authors selected the aluminum element as the substituent in the $BiLaFeO_3$ perovskite system. Then, the chemical formula is confirmed as $Bi_{0.2}La_{0.8-x}Al_xFeO_3$ (x = 0.2, 0.4, 0.6 & 0.8) (BLAFO). The hydro-thermal process is selected at low operating temperatures to synthesize these nanoparticles. It possesses a few significant benefits like easy preparation, less time-consuming, low operating temperatures, inexpensive, good crystallinity, high homogeneity, etc.

2. EXPERIMENTAL

2.1 The Chemicals and Materials

For the synthesis of $Bi_{0.2}La_{0.8-x}Al_xFeO_3$ (x = 0.2, 0.4, 0.6 & 0.8) (BLAFO) (Fig. 1) nanoparticles, the hydrothermal method is preferred. As a part of this, the raw materials were considered to be $La(NO_3)_{3.6}H_2O$ (99.8 % purity, Sigma-Aldrich), $Al(NO_3)_{3.9}H_2O$ (99.8 % purity, Sigma-Aldrich), $Bi(NO_3)_{3.5}H_2O$ (99.8 % purity, Sigma-Aldrich), and $Fe(NO_3)_{3.9}H_2O$ (99.9 % purity, Sigma-Aldrich). The details of the preparation method can be seen in [2].

2.2 Characterization Methods

Samples are shown in Fig. 1. The characterization is carried out by XRD, TEM, SEM, UV-visible spectrometer, Vibrating sample magnetometer VSM, P-E loop (Marain

* Correspondence e-mail: bk_1381@rguktn.ac.in

Cite this article as: S. Perugu et al., *J. Nano- Electron. Phys.* 17 No 1, 01009 (2025) https://doi.org/10.21272/jnep.17(1).01009

India Ltd.), and LCR controller (HIOKI 3532-50, 42 Hz– 5 MHz) to study the structural, morphological, optical band gap, magnetic, ferroelectric, and dielectric properties, respectively.

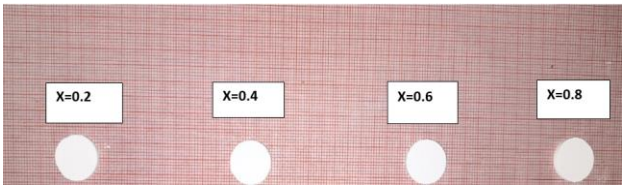

Fig. 1 – The photos of prepared BLAFO samples

3. RESULTS AND DISCUSSIONS

3.1 Structural Characterization

The XRD patterns (Fig. 2) of $Bi_{0.2}La_{0.8-x}Al_xFeO_3$ ($x = 0.2$, 0.4, 0.6 & 0.8) (BLAFO) nanoparticles showed high crystallinity nature about the trigonal phases along with secondary phases related to aluminum titanate, and rutile. The primary phases agree with the standard JCPDS: 86-1518. Usually, the secondary phases can be created due to two factors.

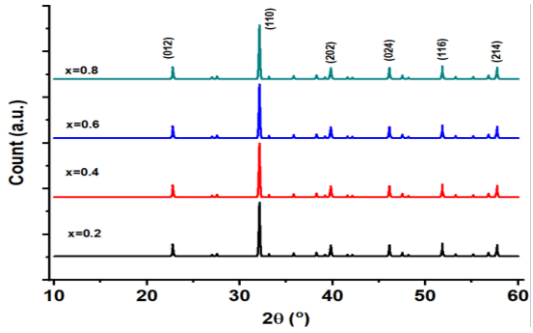

Fig. 2 – XRD patterns of BLAFO nanoparticles

One is due to the incomplete reaction, and the other is the compound's high ionic radii difference of cations. Herein, the reaction is completed successfully. The ionic radii of cations can be considered as La^{+3}: 0.136 nm, Bi^{+3}: 0.096 nm, Al^{+3}: 0.039 nm, Fe^{+3}: 0.0645 nm [11]. It is understood from the ionic radii that the ionic radii difference is greater than 15 %. Hence, the secondary phases will be formed according to the Hume-Rothery rule [12, 13]. However, upon substituting the aluminum, the high ionic radii difference leads to fluctuation in the structure. This implies that an unstable structure will be formed. Hence, the aluminum cations will form secondary phases related to aluminum titanate. The average crystallite size was determined using the Scherrer equation: $D = 0.9\,\lambda / \beta \cos\theta$, where '$\beta$' is the full-width half maxima, and 'θ' is the angle of diffraction [14], and the results were found to be increasing from 86.4 to 31.5 nm as a function of composition from $x = 0.2$ to 0.8. This trend can be ascertained due to the increasing internal microstrain during the hydrothermal reaction. The lattice constants were decreased from 0.5624 – 0.5600 nm ($a = b$) and 1.3968 – 1.3914 nm (c) owing to the low ionic radii of the substituted element. A constant c/a ratio was obtained for all the samples, about 2.483. Further, the unit cell volume ($V = a2c$) was decreased from 0.441 – 0.436 nm^3 with an increase in 'x'. The theoretical density was calculated using the formula $\rho_x = Z \times M \times W/N \times V$ (for trigonal $Z = 1$, where Z – effective number of atoms per unit cell, $M.W$ is the molecular weight of the composition, N is the Avogadro's number (6.023×10^{23}), and V is the unit cell volume). The results were mentioned in Table 1, and it was observed that the values were decreased from 0.760 – 0.514 g/c.c., with 'x'. This kind of low densities were common in as synthesized nanoparticles as they were not processed for any calcination or sintering. Moreover, it was known that the bulk materials show high density due to less porous structure, whereas the nanomaterials will have high dislocation density, indicating low density. In the current work, the molecular weight was decreased from 202.379 to 135.224 g/mol., as a function of 'x'. This could be the reason for the decrease in density. The surface area S of $x = 0.2 – 0.8$ samples increased from 91.30 to 370.19 m^2/g. This happens due to the decrease in crystallite size.

Table 1 – Structural analysis of BLAFO nanoparticles

x	0.2	0.4	0.6	0.8
D (nm)	86.4	60.2	42.8	31.5
$a = b$ (nm)	0.5624	0.5614	0.5608	0.56
c (nm)	1.3968	1.3945	1.3927	1.3914
c/a ratio	2.483	2.483	2.483	2.484
MW (g/mol)	202.379	179.994	157.609	135.224
V_{cell} $(nm)^3$	0.441	0.439	0.438	0.436
ρ_x (g/cm^3)	0.760	0.679	0.597	0.514
P_{avg} (nm)	121.33	104.9	82.1	71.1
G_{avg} (nm)	152.33	137.48	119.24	102.81
S (m^2/g)	91.30	146.57	234.64	370.19

It was familiar that surface morphology can be understood using FESEM and HRTEM. The FESEM images are shown in Fig. 3.

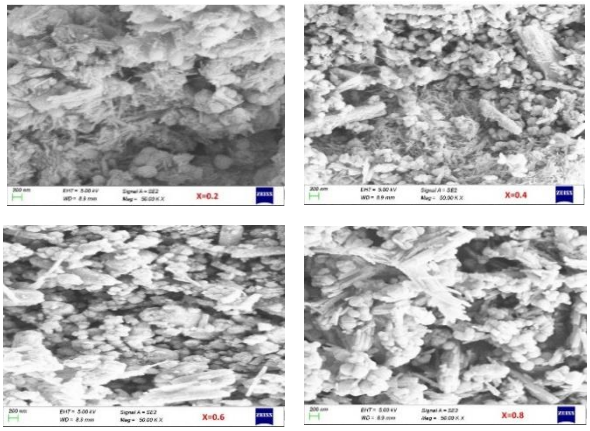

Fig. 3 – FESEM images of BLAFO nanoparticles

The images evidenced that all samples contain nanosphere grains, including the nanorods-like structures. This can happen due to the nucleation process, wherein the nanospheres are deformed owing to predominant vibrations. These vibrations or fluctuations will be set up to the morphological species. It was seen that the nanorods were larger in number at low aluminum content. The nanorods came down with increased aluminum content, and subsequently, the nanospheres were increased. This established that the vibrations were reduced upon increasing the aluminum content. The average grain size was determined using the linear intercept method, wherein the formula $G_{avg} = 1.5\ L / MN$ (where L indicates the test line length, M indicates the magnification, and N indicates the number of grains intersecting the test line) was used. The average grain size values were noted to be decreased from 152.33 to 102.81 nm with 'x.' Similarly, the HRTEM (Fig. 4) images showed the nanospheres and nanorods-like species in the morphology. The nanorods were reduced, and nanospheres were increased with Al-content increase. The HRTEM results agreed with the FESEM results. The average particle size was calculated and noticed to be decreasing from 121.33 to 71.1 nm as a function of 'x'. From the obtained data on average crystallite size, grain size, and particle size, it was clear that the grain size is bigger than all. That means the grains contain particles, and the particles contain crystallites. Hence, the diameters of grains, particles, and crystallites de-creased in the nanosamples.

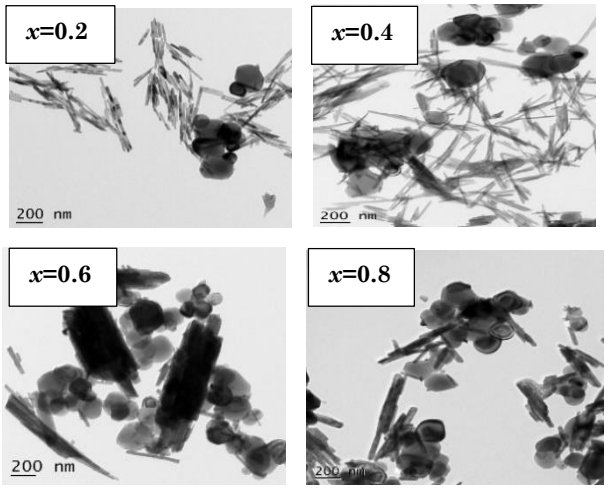

Fig. 2 – HRTEM images of BLAFO nanoparticles

The frequency dependence of dielectric parameters such as dielectric constant (ε'), and dielectric loss (ε'') is discussed as a function of Al-content. For this $\varepsilon' - \log \omega$, and $\varepsilon'' - \log \omega$ plots were drawn as shown in Figs. 5 (a-b), respectively.

The dielectric constant of $x = 0.2 - 0.8$ samples was observed to be high in magnitude at low frequencies. This is attributed to the inhomogeneous dielectric structure. According to Koop's double layer theory, it was understood that polycrystalline materials contain two layers,

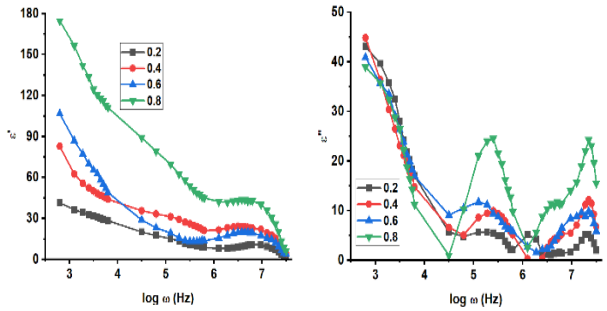

a b

Fig. 5 – (a) $\varepsilon' - \log \omega$ plots of BLAFO nanoparticles, (b) $\varepsilon'' - \log \omega$ plots of BLAFO nanoparticles

such as grain and grain boundary. The grains are usually low resistive or high conductive, and grain boundaries are high resistive or conductive. In the present case, the high value of dielectric parameters is obtained due to grain boundary contribution. At low applied electric field frequency, the charge carriers can be piled up at the grain boundary interface [15-17]. Herein, the energy of the grain boundary is greater than the energy of carriers. Hence, the probability of tunneling charge carriers through grain boundaries is very low. Therefore, the polarizations increased due to the accumulation of carriers. We refer to this polarization as space charge or electrode or Maxwell-Wagner polarization. The carriers will receive the excess energy once the input electric field frequency is increased. Hence, the energy of carriers will be now greater than the energy of grain boundary. Therefore, the carriers can break the grain boundary and enter the grain portion. Then, the resistance will automatically come down, increasing conductivity. At megahertz frequency, the $x = 0.2 - 0.8$ samples expressed the Debye relaxations with changing relaxation frequencies. These were changed between 6.845 to 7.102. With the increase of Al-content, the dielectric constant was increased. The $x = 0.8$ content showed a high dielectric constant of about 6.15. The dielectric loss versus frequency plots offered high dielectric loss values at low frequencies, which gradually decreased with the in-crease in frequency. This occurs due to the dispersion of dielectric behavior. However, the plots offered two consecutive Debye relaxations at around 5.5 and 7.5. The dielectric loss values were increased with 'x', and the high magnitude was found at $x = 0.8$. This value is about 15.2 (Table 2). This result confirmed that the $x = 0.8$ sample, due to its high dielectric constant and high dielectric loss, can be suitable for dielectric absorber applications.

Table 2 – Data on dielectric parameters of BLAFO nanoparticles

x	0.2	0.4	0.6	0.8
		ε'		
8 MHz	1.88	4.92	4.10	6.15
		ε''		
8 MHz	1.97	6.7	5.49	15.2

Similarly, the frequency variation of ac-electrical conductivity was depicted in Fig. 6.

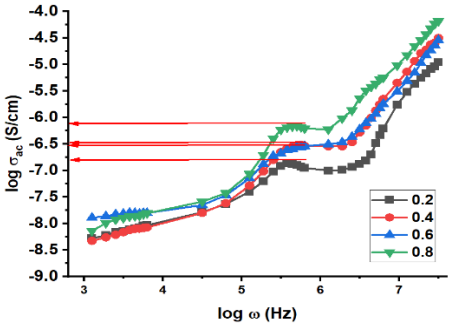

Fig. 6 – logσ_{ac} – log ω plots of BLAFO nanoparticles

It was found that the ac-conductivity was increased with frequency. This occurs owing to the hopping of the conduction mechanism. The frequency-independent region is found for the applied log ω values of 5.5 to 6.0. This region indicates the dc-conducting region. The dc-conductivity values were identified by extrapolating the frequency-independent portion of the plots toward the *Y*-axis.

The magnetic permeability of $x = 0.2 – 0.8$ samples was studied with frequency (Fig. 7).

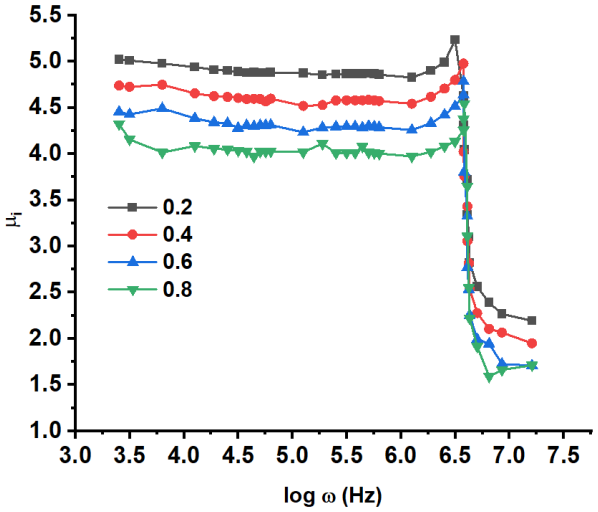

Fig. 7 – μ_I – log ω plots of BLAFO nanoparticles

All samples' initial permeability ($\mu_I = L / L_o$) showed a constant trend up to log $\omega = 6.0$. Above this frequency, the samples showed an abrupt increase in permeability to maximum values. The peak positions of permeability values increased from log $\omega = 6.5 – 6.75$. After these positions, the sudden drop off of the permeability was noticed. This trend follows Snoke's law, wherein the maximum value will be obtained at the peak position, and minimum values will be found above the peak position.

At the peak position, the input magnetic field frequency of toroidal samples matches the frequency of the oscillating magnetic dipoles. Then, the resonance will take place, inducing the magnetic permeability. The compositional dependence of permeability suggested that the permeability values were decreased upon increasing the Al-content in the perovskite system. Moreover, the sudden and sharp drop off of the samples indicated the high homogeneity nature of the samples. In Fig. 8, the *M-H* loops were shown, and the trend was almost un-saturated. Hence, the maximum magnetization could be determined.

The saturation magnetization (M_s) was found using the LAS plots (Fig. 9).

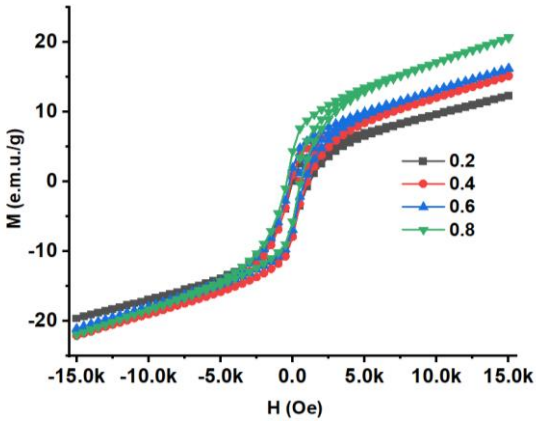

Fig. 8 – *M-H* curves of BLAFO nanoparticles

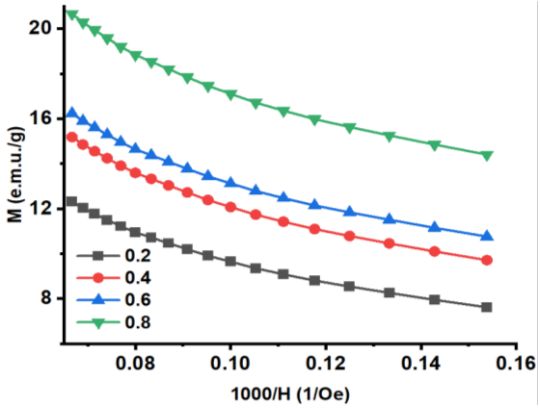

Fig. 9 – LAS plots of BLAFO nanoparticles

The results were reported in Table 3. The M_s values were increased from 12.56 to 20.89 emu/g as a function of '*x*'. The retentivity M_r was varying unsystematically. Later, the squareness (M_r/M_s) values were computed and found to be altering from 0.222 – 0.076. This evidenced that the M_r/M_s values were less than 0.5, as we know that the multi-domain magnetic nanoparticles will indicate the squareness values as less than half. That means the present BLAFO nanoparticles can be multi-domain magnetic [18]. Later, the anisotropy constant $K_1 = H_c M_s$ / 0.96 and magnetic moment $n_B = M.W. * M_s$ / 5585 [19] were calculated and listed in Table 3.

The results ensured that the K_1 varied from 9859 – 4689 erg/c.c., with '*x*' unsystematically. Likewise, the magnetic moment also varied from 0.455 – 0.505 μB/f.u., with an increase in '*x*'. This behavior

was attributed to the decrease of compositional molecular weight as listed in Table 1. Further, the ferroelectric hysteresis nature of $x = 0.2 – 0.8$ was analyzed using the *P-E* loops (Fig. 10). It was observed from the *P-E* loops that the 'banana' shape was predominant for $x = 0.2 – 0.8$.

Table 3 – Magnetic parameters of BLAFO nanoparticles

x	0.2	0.4	0.6	0.8
M_s (emu/g)	12.56	15.31	16.42	20.89
M_r (emu/g)	2.34	3.41	2.12	1.59
M_r/M_s	0.186	0.222	0.129	0.076
H_c (Oe)	358.45	618.23	302.47	326.89
K_1 (erg/c·c)	4689.72	9859.48	5173.50	7113.26
n_B (μB)	0.455	0.493	0.463	0.505

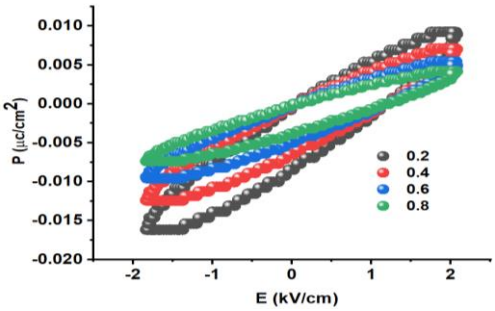

Fig. 10 – P-E loops of BLAFO nanoparticles

This indicated that the oxygen vacancies seemed to be high in concentration. Due to this, the 180° ferroelectric spins will be predominant. A similar nature was discussed earlier by several scientists [20]. Moreover, this showed the weak ferroelectric nature wherein the bismuth cations could be responsible for this nature.

4. CONCLUSION

$Bi_{0.2}La_{0.8-x}Al_xFeO_3$ ($x = 0.2$, 0.4, 0.6 & 0.8) (BLAFO) nanoparticles were synthesized via hydrothermal technique. The XRD confirmed the trigonal phases about some secondary phases related to aluminum titanate and rutile. The morphology evidenced the formation of nanorods-like structures due to the nucleation process. The dielectric properties established that the $x = 0.8$ sample showed high dielectric constant (6.15), and high dielectric loss (15.2). This composition can be suitable for dielectric absorber applications. The ac-conductivity versus frequency plots showed the frequency-independent region around log ω values of 5.5 to 6.0. The M-H loops showed a decreasing trend of magnetization from 12.56 to 20.89 emu/g as a function of '*x*.' The squareness (M_r/M_s) values were computed and found to be altering from 0.222 – 0.076, indicating the M_r/M_s values were less than 0.5. Hence, the present BLAFO nanoparticles can be of a multi-domain magnetic nature. All the samples show that the ferroelectric loops go banana-shaped.

REFERENCES

1. Y. Li, H.J. Yang, W.G. Yang, Z.L. Hou, J.B. Li, H.B. Jin, J. Yuan, M.S. Cao, *Mater. Lett.* **111**, 130 (2013).
2. M. Gowrishankar, D. Rajan Babu, P. Saravanan, *Mater. Lett.* **171**, 34 (2016).
3. A.T. Apostolov, I.N. Apostolova, J.M. Wesselinowa, *J. Magn. Magn. Mater.* **513**, 167101 (2020).
4. S.P. Balmuchu, P. Dobbidi, *Physica B: Condens. Matter* **638**, 413937 (2022).
5. X. Zhang, C. Zhang, N. Ran, *Mater. Lett.* **179**, 186 (2016).
6. Y. Wang, *Solid State Commun.* **341**, 114595 (2022).
7. P. Kumar, P. Chand, V. Singh, *Chem. Phys. Lett.* **754**, 137715 (2020).
8. P. Priyadharsini, A. Pradeep, B. Sathyamoorthy, G. Chandrasekaran, *J. Phys. Chem. Solids* **75**, 797 (2014).
9. F. Pedro-García, L.G. Betancourt-Cantera, A.M. Bolarín-Miró, C.A. Cortés-Escobedo, A. Barba-Pingarrón, F. Sánchez-De Jesús, *Ceram. Int.* **45**, 10114 (2019).
10. S. Kumar, G. Srivastava, G. Almutairi, F. Ahmed, N.M. Shaalan, S. Dalela, R. Kumar, A.P. Kumar, P.A. Alvi, K.H. Chae, H.H. Hammud, K. Kumari, *J. Electron Spectroscopy Related Phenomena* **253**, 147138 (2021).
11. R.D. Shannon, *Acta Cryst. A* **32**, 751 (1976).
12. Hume-Rothery Rules, *Van Nostrand's Scientific Encyclopedia* (John Wiley & Sons, Inc.: 2002).
13. S. Dastagiri, G. Pakardin, T.A.Babu, M.V. Lakshmaiah, K.C.B. Naidu, *J. Mater. Sci.: Mater. Electron.* **32**, 8017 (2020).
14. P. Scherrer, *Mathematisch-Physikalische Klasse* **2**, 98 (1918).
15. S. Dastagiri, M.V. Lakshmaiah, C.B.K. Naidu, *J. Mater. Sci: Mater. Electron.* **30**, 20253 (2019).
16. K.C.B. Naidu, T.S. Sarmash, M. Maddaiah, P.S. Reddy, D.J. Rani, T. Subbarao, *Journal of the Australian Ceramic Society* **52** (2016).
17. K.C.B. Naidu, T.S. Sarmash, V.N. Reddy, M. Maddaiah, P.S. Reddy, T. Subbarao, *Journal of the Australian Ceramic Society* **51**, 94 (2015).
18. N. Raghuram, T.S. Rao, K.C.B. Naidu, *Appl. Phys. A* **125**, 839 (2019).
19. D.B. Basha, N.S. Kumar, C.B.K. Naidu, *Sci. Rep.* **12** 12723 (2022).
20. N.S. Kumar, R.P. Suvarna, K.C.B. Naidu, *J. Mater. Sci.: Mater. Electron.* **29**, 4738 (2018).

Структура, морфологія та мультифероїчні властивості наночастинок $Bi_{0.2}La_{0.8-x}Al_xFeO_3$ (x = 0.2, 0.4, 0.6 & 0.8)

S. Perugu[1], G.B. Kiran[2], T.A. Bbau[3], B.V. Raghavaiah[4]

[1] *Department of Physics, Acharya Nagarjuna University, Guntur-522510, India*
[2] *Department of Mechanical Engineering, Rajiv Gandhi University of Knowledge Technologies (RGUKT), Nuzvid-521201, India*
[3] *Department of Physics, Andhra University, Visakhapatnam-530003, India*
[4] *Department of Physics, Rajiv Gandhi University of Knowledge Technologies (RGUKT), Ongole-523001, India*

У даній дослідницькій роботі наночастинки $Bi_{0.2}La_{0.8-x}Al_xFeO_3$ (x = 0.2, 0.4, 0.6 & 0.8) (BLAFO) були отримані за допомогою гідротермальної техніки. На рентгенівських дифрактограмах спостерігались тригональні фази та вторинні фази, пов'язані з наявністю титанату алюмінію і рутила. Зображення FESEM і HRTEM показали утворення наностижневих структур внаслідок процесу зародження. Діелектричні властивості виражають поляризацію просторового заряду та релаксації типу Дебая на частотно-залежних графіках діелектричної проникності. Подібним чином, графіки залежності діелектрика від частоти показали численні релаксації. Криві магнітного гістерезису вказують на тенденцію до зменшення намагніченості та магнітного моменту. На залежностях LAS наведена намагніченість насичення. Сегнетоелектричні петлі гістерезису для всіх зразків мають форму «банана».

Ключові слова: Наночастинки, Мультифероїк, Структура, Мікроскопія, Діелектрична проникність.